Reynolds and dispersive shear stress in free-surface turbulent channel flow over square bars

Razieh Jalalabadi* and Thorsten Stoesser
Civil, Environmental and Geomatic Engineering, University College London, Gower Street, London WC1E 6BT, United Kingdom

(Received 30 March 2021; accepted 9 February 2022; published 8 March 2022)

Reynolds and dispersive shear stresses in turbulent flow over spanwise-aligned square bars in an open channel flow are examined. Results of large-eddy simulation of flow over two different bar spacings corresponding to transitional and k-type (reattaching flow) roughness are analyzed. The Reynolds shear stress contribution to the momentum loss (or the friction factor, respectively) is greater than the dispersive shear stress contribution. By increasing the bars spacing, however, the contribution of the dispersive shear stress increases while the Reynolds shear stress contribution decreases, which is due to a standing wave at the water surface in the flow over k-type roughness which results in significant spatial variations in the time-averaged velocities. Strong sweep events take place and contribute to the friction coefficient. Investigating the dynamics of the flow reveals that there is momentum source below the crest of the bars and momentum sink above them, leading to acceleration or deceleration of flow, respectively. The contribution of dispersive shear stress is significant only in the deceleration of the flow near the crest of the bars and in the acceleration of the flow under the water surface. Quantification of the three components of total kinetic energy, i.e. mean, turbulent, and wake kinetic energy, reveals that the largest contribution is that of the mean flow in both geometries. By increasing the bar spacing, the contributions of turbulent and wake kinetic energy, which are localized at the bar height, increase, while the kinetic energy of the mean flow decreases.

DOI: 10.1103/PhysRevE.105.035102

I. INTRODUCTION

Turbulent flows over rough surfaces are of critical and fundamental importance in engineering applications. The flow dynamics is altered by surface roughness mainly through the change of the mean velocity profile near the wall which leads to the modification of the friction coefficient [1]. Where the maximum roughness height is not negligible with respect to the integral length of the flow, the flow modification is not limited to the viscous and buffer layers but extends to the logarithmic layer where at least half of the turbulent energy is produced. In free-surface shallow flows over rough beds, the roughness and topography of the bed (among other factors) is "felt" all the way to the water surface. In such low relative submergence flows, direct interaction of bed and water surface takes place through the alteration of the bulk flow. Scrutinizing the bulk flow structure leads to a detailed understanding of the flow characteristics and quantities such as momentum transport and friction coefficient.

Attaching roughness to the surface alters the flow structure either directly or through the modification of near wall dynamics. In order to incorporate the spatial heterogeneity induced by the roughness in the averaged parameters, the double-averaging methodology was introduced [2,3]. In this method, the time averaging which yields the Reynolds-averaged Navier-Stokes (RANS) equations is supplemented by spatial averaging, which yields the double-averaged Navier-Stokes (DANS) equations [4,5]. Dispersive or form-induced shear stresses are a result of double averaging and represent the spatial variations in the time-averaged velocity field. These stresses are induced by near-bed flow heterogeneity and secondary currents when roughness is present. The double-averaged (DA) statistics have been studied in several works for wall-bounded canonical flows over rough surfaces with irregular and regular geometrical roughness elements. The dispersive stresses are reported to be generally smaller than the corresponding Reynolds stresses for different surface morphologies, except for the normal streamwise dispersive stress for which the peak value is comparable to its Reynolds stress counterpart [6–8], yet it significantly depends on geometrical surface parameters [6]. The peak magnitudes of dispersive stresses occur under or around the roughness crest and at some distance away from the roughness crest they are negligible, unlike the Reynolds stresses. Over a specific irregular roughness, both dispersive and Reynolds stress peak magnitudes increase by increasing the Reynolds number [8]. The wall-normal gradient of dispersive shear stress is comparable to the wall-normal gradient of Reynolds shear stress and by increasing the Reynolds number the relative difference in the peak magnitudes of these stresses decreases [8–10]. The sign of the wall-normal gradient of these stresses is different, highlighting their different contribution to momentum transport.

Among multiple roughness types, square bars perpendicular to the main flow direction have been an area of intense research as this canonical configuration allows studying the principal effects of surface roughness on flow characteristics [11–14]. The bar spacing is a key parameter of this roughness geometry and the main two types of this roughness, as first identified by Perry *et al*. [15], are d-type (closely

*r.jalalabadi@ucl.ac.uk

 ©2022 American Physical Society

spaced bars) and k-type (widely spaced bars) roughness. In the former, the bulk flow skims over the bars while a stable vortex is formed between the bars. In the latter, flow separation and flow reattachment downstream of a bar take place. At around $\lambda/k = 4$–5, the transition from d-type to k-type roughness occurs, where k is the bar height and λ is the bar spacing [1,16,17].

The alteration of the friction coefficient due to surface roughness is generally in the form of an increase. The potential of energy saving by drag reduction due to surface manipulation has led to a multitude of research over the past few decades [18]. Many other studies investigated the decomposition of the friction coefficient into its constituents with the aim to quantify the effects of flow structure on the generation of the total drag. The main approaches to implement this decomposition are based on the momentum budget [19,20], energy budget [10,21], and velocity-vorticity correlation [22–24]. Triple integration of momentum, kinetic energy, or vorticity equations are carried out in these approaches to calculate the decomposition of the friction factor. Among all these methods, the work of Nikora *et al*. [20] is suitable for both smooth and rough walls, which accounts for roughness-scale flow separation and the emergence of pressure drag at the bed. Furthermore, in their approach, the direct contribution of Reynolds and dispersive stresses to the generation of the Darcy-Weisbach friction factor, being widely used in hydraulics application, is presented.

The objective of the present work is to quantify Reynolds and dispersive shear stresses in free-surface turbulent flow over transitional and k-type transverse square-bar roughness. The underlying data are generated by large-eddy simulations. The spatially varying contributions of the Reynolds and dispersive stresses to the integral friction coefficient are explored and compared. The distribution of these stresses and the physical phenomena resulting these distributions are scrutinized. The budgets of turbulent inertia and kinetic energy are investigated as well to quantify the contribution of the Reynolds and dispersive stresses. This manuscript is organized into four sections. In Sec. II, the numerical method and details of the simulations are described. Section III presents and discusses the results and the conclusion is presented in Sec. IV.

II. NUMERICAL SIMULATIONS

Turbulent flow in a rough-bed open channel is simulated using the method of large-eddy simulation (LES). The in-house LES code HYDRO3D, which has been validated thoroughly for a large number of flows with similar complexity [25–30], is employed to solve the spatially filtered Navier-Stokes equations,

$$\nabla \cdot \mathbf{u} = 0, \tag{1}$$

$$\frac{\partial \mathbf{u}}{\partial t} + \mathbf{u} \cdot \nabla \mathbf{u} = -\nabla p + \frac{1}{\mathrm{Re}} \nabla^2 \mathbf{u} - \nabla \cdot \tau. \tag{2}$$

Here, $\mathbf{u}$ is the velocity vector with the three components u, v, w in the streamwise (x), spanwise (y), and wall-normal (z) directions, p is the pressure, $\mathrm{Re} = U_b H/\nu$ is the Reynolds number where U_b is the bulk velocity, H is the depth defined as the distance between the mean water surface position before starting the simulation and the mean bed elevation (z_{mb}), ν is the fluid kinematic viscosity, and $\boldsymbol{\tau}$ is the subgrid scale stress tensor. A fractional-step method with a second-order Runge-Kutta time integration scheme is used to solve equations on a staggered Cartesian grid. In the predictor step, a second-order central differencing method is used to compute diffusive terms. The convective terms are computed using a fifth-order weighted, essentially nonoscillatory (WENO) scheme to compromise between numerical accuracy and algorithm stability [27]. In the corrector step, the pressure Poisson equation is solved using a multigrid method to achieve a divergent flow field at the end of each time step. The wall-adapting local eddy-viscosity (WALE) model is used to approximate the effects of the small-scale turbulence on the large eddies [31]. The free surface is captured using the level set method (LSM), which is successful in the description of complex air-water interfaces [32,33]. In this method, the interface is tracked by solving a pure advection equation for a level set signed distance function which is zero at the phase interface, negative in air, and positive in water. The sudden changes of density and viscosity of the two immiscible fluids at either side of the free surface may cause instability. To avoid this, a transition zone with the thickness of two grid spacings is introduced at either side of the phase interface where density and viscosity are calculated using a Heaviside function. The governing equations are solved via parallel computing, and Message Passing Interface (MPI) is used for this purpose. More details of the code can be found in [34,35]. Table I provides geometrical and hydraulic parameters for the two simulated cases. Two different bar spacings are considered: $\lambda/k = 5.2$ is considered transitional (wake interference flow) roughness as it is neither d-type (skimming flow) nor k-type (reattaching flow) roughness, and $\lambda/k = 10.4$ is classified as k-type roughness. In terms of k^+, both flows can be considered hydraulically rough (see Table I). Only these two roughness types are considered since, unlike the skimming flow, in these cases significant momentum transfer takes place between the area below the crest of the bars and the bulk flow [36]. Figure 1

TABLE I. Hydraulic conditions and computational details.

λ/k	H/k	U_b	Re	Fr	(L_x, L_y, L_z)	Δx^+	Δy^+	Δz^+	k^+
5.2	2.5	0.24	7.2×10^3	0.44	$(10.4k, 5k, 5k)$	5.6	6.6	3.5	84.0
10.4	2.9	0.23	8.0×10^3	0.39	$(10.4k, 5k, 5k)$	5.5	6.5	3.5	82.8

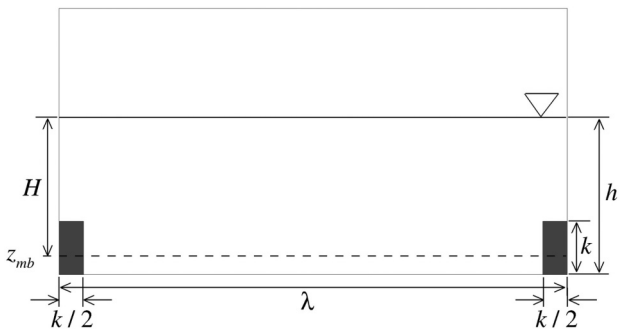

FIG. 1. Schematic of the computational domain.

presents the schematic of the computational domains. As the length of the domain, L_x, for both bars spacings is similar, the domain includes two troughs for the $\lambda/k = 5.2$ case and one trough for the $\lambda/k = 10.4$ case. The adequacy of the domain size for both cases is evaluated using two-point correlation of the streamwise velocity fluctuations in the streamwise and spanwise directions and is not shown for brevity. The Re and global subcritical Froude number, $\mathrm{Fr} = U_b/\sqrt{gH}$, are similar for both cases (g is the gravity acceleration). In both cases, the grid spacing is uniform in all directions because it minimizes dispersive discretization errors in the high-order numerical schemes that are employed and allows high-accuracy predictions of water surface deformations. The grid is sufficiently fine to resolve the small-scale turbulent motions (Table I), as was shown in [30]. The flows are driven by a constant pressure gradient of similar value to the flume experiments discussed in [30]. A no-slip boundary condition is applied at the bed and at the surface of the bars. The no-slip condition on the surface of the bars is enforced in every time step by setting the velocity at the first grid point inside the bar to the negative value of the first grid point outside the bar, hence ensuring the velocity to be exactly zero at the boundary. Periodic boundary conditions are applied in the streamwise and spanwise directions, thus the flow is quasi-two-dimensional and homogeneous in the spanwise direction. All simulations are initiated with a free-slip boundary condition at the still water level and, after attaining a fully developed flow, the simulations are restarted with the level set algorithm to track the free surface. When the free-surface flow is fully developed again, averaging of the flow quantities is begun and continued for between 40 and 60 further flow through periods to obtain converged turbulence statistics. In this work, small symbols are instantaneous quantities, time-averaged quantities are denoted with an overbar, small symbols with prime are turbulent fluctuations, the double- (temporal- and spatial-) averaged quantities are denoted by both the overbar and brackets $< >$, and the dispersive quantities that represent the spatial fluctuations of the time-averaged quantities are denoted by a tilde. Thus, an instantaneous flow variable is decomposed as

$$\theta(x, y, z, t) = \langle\overline{\theta}\rangle(z) + \widetilde{\theta}(x, y, z) + \theta'(x, y, z, t). \tag{3}$$

A DA variable is calculated using the volume-averaging operator applied to the temporally averaged variable as

$$\langle\overline{\theta}\rangle(z) = \frac{1}{\phi(z)}\frac{1}{V_o}\iiint_{V_f} \overline{\theta}(x, y, z)\, dx\, dy\, dz. \tag{4}$$

Here, $\phi = V_f \,/\, V_o$ is the geometry function, where V_f is the volume occupied by the fluid and V_o is the total volume. The averaging volume is a thin slab parallel to the bed with the size $L_x \times L_y \times \Delta z$ and it is larger than the dominant roughness scale [5,37]. The dispersive and Reynolds shear stresses are calculated as [38]

$$\tilde{u}\tilde{w} = (\overline{u} - \langle\overline{u}\rangle)(\overline{w} - \langle\overline{w}\rangle), \tag{5}$$

$$\overline{u'w'} = \overline{(u - \overline{u})(w - \overline{w})}. \tag{6}$$

The superscript $+$ in this work represents inner-scaled quantities calculated using the friction velocity $u_\tau = \sqrt{\tau_{\mathrm{wall}}/\rho}$, where τ_{wall} is the wall shear stress and ρ is the water density.

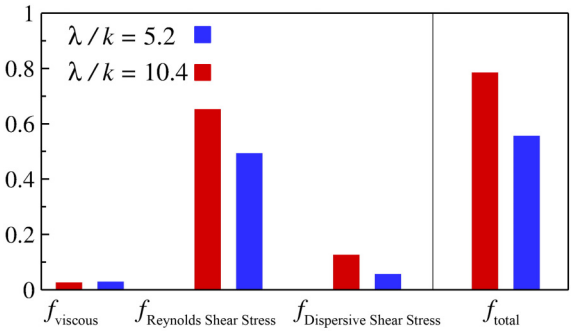

FIG. 2. Contributions to friction factor f.

The adequacy of the grid and validation of the results have been demonstrated previously [39] using the experimental and numerical data of McSherry *et al*. [30].

III. RESULTS AND DISCUSSION

A. Friction factor decomposition

The momentum-based method proposed by Nikora *et al*. [20] is applied to quantify the contribution of viscous effects, as well as Reynolds and dispersive shear stresses, to the Darcy-Weisbach friction factor $f = 8\tau_0/(\rho U_b^2)$, where $\tau_0 = \int_{z_t}^{z_c} F_D\, dz$ and F_D is the total drag applied on the bed. For steady, two-dimensional flow over a rough bed, the friction factor computes from

$$f = \underbrace{\frac{48}{\mathrm{Re}}\frac{1}{N}}_{f_{\mathrm{viscous}}} + \underbrace{\frac{48}{Q^2 N}\int_{z_t}^{z_{ws}} (z_{ws} - z)\phi\langle -\overline{u'w'}\rangle\, dz}_{f_{\mathrm{Reynolds\ shear\ stress}}} + \underbrace{\frac{48}{Q^2 N}\int_{z_t}^{z_{ws}} (z_{ws} - z)\phi\langle -\tilde{u}\tilde{w}\rangle\, dz}_{f_{\mathrm{dispersive\ shear\ stress}}}. \tag{7}$$

Here, $N = 3(L_\tau/H)^2 + (\tau_{02D})/(\tau_0)(L_\phi/H)^3$ - $(h/H)^3$ is a parameter characterizing flow–rough-bed interaction, where $L_\tau = [\int_{z_t}^{z_c}(z_{ws} - z)^2 F_D\, dz / \int_{z_t}^{z_c} F_D\, dz]^{0.5}$ is a drag length scale, $\tau_{02\mathrm{D}} = \rho g H S_b$ while S_b is bed slope, $L_\phi = [3\int_{z_t}^{z_{ws}}(z_{ws} - z)^2(1 - \phi)\, dz]^{1/3}$, and $Q = U_b H$. Here, z_{ws}, z_t, and z_c are water surface elevation, roughness trough elevation, and roughness crest elevation, respectively. More details for the calculation of these terms can be found in [20]. The contribution of each term in Eq. (7) to f is presented in Fig. 2. As expected, the viscous contribution is the smallest and the dispersive shear stress contribution is less than that of the Reynolds shear stress for both geometries. The friction coefficient is larger for $\lambda/k = 10.4$ as the flow separates at the bar and reattaches to the bed after the recirculation zone, generating a positive velocity gradient adjacent to the bed, whereas in the flow over $\lambda/k = 5.2$ there is no flow separation

TABLE II. Contributions to the friction factor f.

λ/k	f	f_{viscous}	$f_{\mathrm{Reynolds\ Shear\ Stress}}$	$f_{\mathrm{Dispersive\ Shear\ Stress}}$
5.2	0.57	1.0%	89.0%	10.0%
10.4	0.83	0.6%	81.8%	17.6%

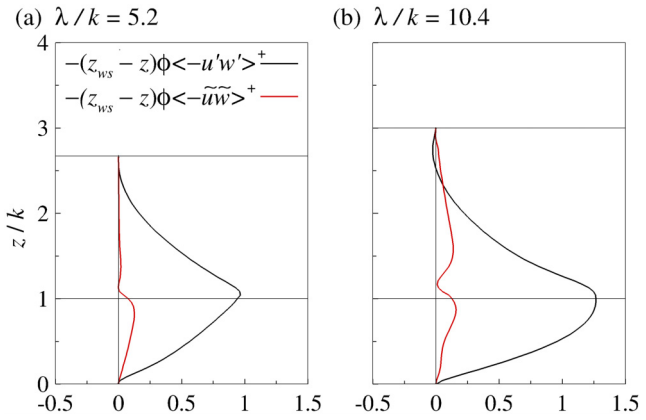

FIG. 3. Integrands representing the contribution of Reynolds and dispersive shear stresses to the friction factor f.

or reattachment between bars [39]. The exact magnitude (in percent of the total) of each contribution is shown in Table II. The difference between f_{total} calculated as the sum of the contributions and f_{total} calculated using the Darcy-Weisbach formulation is less than 10%. By increasing bar spacing, the Reynolds shear stress contribution to f decreases while the dispersive shear stress contribution to f increases. Investigating the wall-normal variations of the integrands in the last two terms in Eq. (7) reveals the contribution of these shear stresses to f at different wall distances. As shown in Fig. 3, the Reynolds shear stress integrand is larger in flow over $\lambda/k = 10.4$ than that in the flow over $\lambda/k = 5.2$. The maximum magnitude of the Reynolds shear stress integrand occurs near the bar crest for both geometries. The dispersive shear stress integrands are similar in both geometries under the crest of the bars having a peak near $z/k = 1$. However, for the flow over $\lambda/k = 10.4$, there is a second peak above the bar, leading to a larger contribution of this stress to f in this case. The distribution and generation of Reynolds and dispersive shear stresses will be examined to explore the reason for these differences.

TABLE III. Magnitudes and locations of maximum Reynolds shear stress.

λ/k	$\langle -\overline{u'w'}\rangle^+_{\text{max}}$	x/k	z/k
5.2	0.83	4.30	0.92
10.4	0.88	3.10	0.83

B. Spatial variation of turbulent and dispersive shear stresses

Figure 4 shows time- and spanwise-averaged normalized Reynolds and dispersive shear stresses in the streamwise–wall-normal plane. In both cases, the Reynolds shear stress is the largest at a wall distance around the bar height. The circles in Fig. 4 represent the location of the maximum $\langle -\overline{u'w'}\rangle^+$, and their magnitudes and locations are mentioned in Table III. These magnitudes and locations are averaged for the two circles in the flow over $\lambda/k = 5.2$. Consistent with Fig. 3, $\langle -\overline{u'w'}\rangle^+_{\text{max}}$ is smaller for $\lambda/k = 5.2$, while in this case, the maximum occurs at larger x/k and z/k. Figure 4(b) shows that the standing wave at the water surface in $\lambda/k = 10.4$ moves this maximum location closer to the bed. As shown in Figs. 4(c) and 4(d), $\langle -\tilde{u}\tilde{w}\rangle^+$ has several positive and negative local peaks in the streamwise direction and the peaks are greater in the flow over $\lambda/k = 10.4$. Above the crest of the bars, however, a large region of strong positive $\langle -\tilde{u}\tilde{w}\rangle^+$ extends from the water surface to the bed, leading to the generation of the second peak in Fig. 3(a). There are local large magnitudes of negative and positive $\langle -\tilde{u}\tilde{w}\rangle^+$ in both geometries at the edges of the bars due to large spatial variations in the time-averaged velocities in these areas.

The normalized components of the dispersive shear stress, $\langle \tilde{u}\rangle^+$ and $\langle \tilde{w}\rangle^+$, are shown in Fig. 5. There are two distinct layers, under and above the bar crest, in the distribution of $\langle \tilde{u}\rangle^+$. Under the crest of the bars, in both geometries, just downstream of the bars where the recirculation bubbles start to develop, $\langle \tilde{u}\rangle^+$ is negative. At the upstream of the bars,

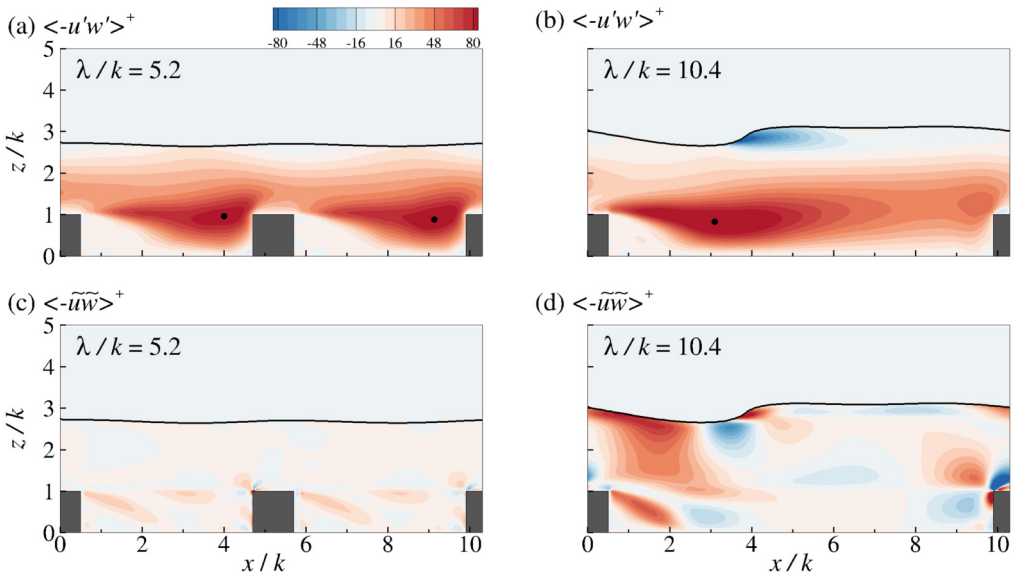

FIG. 4. Contours of time- and spanwise-averaged (a),(b) Reynolds and (c),(d) dispersive shear stress.

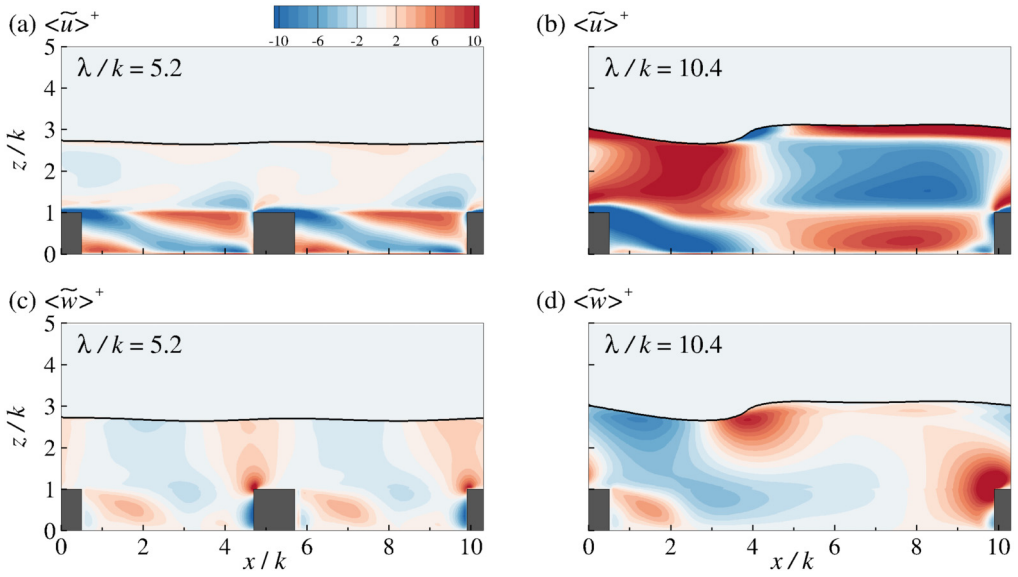

FIG. 5. Contours of temporal- and spanwise-averaged (a),(b) streamwise and (c),(d) wall-normal dispersive velocities.

there is a region of positive $\langle\widetilde{u}\rangle^+$. Above the bar crest, similar regions but with opposite sign are generated. The magnitude of $\langle\widetilde{u}\rangle^+$ is negligible for the $\lambda/k = 5.2$ case above the bar crest. However, in the flow over $\lambda/k = 10.4$, $\langle\widetilde{u}\rangle^+$ is manifested above the bar crest by the changes in water surface elevations. A region of strong positive $\langle\widetilde{u}\rangle^+$ is established at the upstream of the standing wave below the water surface and, at the downstream of this wave, there is a strong negative $\langle\widetilde{u}\rangle^+$ extending downwards to the next bar in the downstream. Figures 5(a) and 5(b) suggest that the changes in $\langle\widetilde{u}\rangle^+$ under the bar crest are due to the presence of the bar, and, above that height, are due to the changes at the water surface. The wall-normal component of $\langle\widetilde{u}\widetilde{w}\rangle^+$ does not have a layered structure. The magnitude of $\langle\widetilde{w}\rangle^+$ is not considerable in the flow over $\lambda/k = 5.2$, except in small areas near the leading edge of the bars. In the flow over $\lambda/k = 10.4$, there are regions of strong positive and negative $\langle\widetilde{w}\rangle^+$ signifying the main effects of the changes in the water surface elevations on $\langle\widetilde{w}\rangle^+$. The negative $\langle\widetilde{w}\rangle^+$ at the upstream of the standing wave expand to the bed. These results show that due to the small changes in the water surface elevation in the flow over $\lambda/k = 5.2$, the weak $\langle\widetilde{w}\rangle^+$ leads to the generation of weak $\langle-\widetilde{u}\widetilde{w}\rangle^+$ [Fig. 4(c)] both above and under the bar crest. In the flow over $\lambda/k = 10.4$, both $\langle\widetilde{u}\rangle^+$ and $\langle\widetilde{w}\rangle^+$ contribute to the generation of stronger $\langle-\widetilde{u}\widetilde{w}\rangle^+$ [Fig. 4(d)] as a result of larger changes in the water surface elevation, with $\langle\widetilde{u}\rangle^+$ being larger than $\langle\widetilde{w}\rangle^+$.

A quadrant analysis is carried out to investigate and quantify the contribution of velocity fluctuations to the generation of Reynolds and dispersive shear stresses. Using this analysis, the shear stresses are divided into four events based on the sign of their fluctuating components [40]. The second and fourth quadrants, $Q2^+(u' < 0, w' > 0)$ and $Q4^+(u' > 0, w' < 0)$, are the dominant events in the turbulent flows and are known as ejection and sweep events, respectively. Ejection events correspond to vertical flow away from the wall ($w' > 0$) at low speed ($u' < 0$) and sweep events are flows towards the wall ($w' < 0$) at high speed ($u' > 0$). Table IV provides the contributions of these four events to the shear stress and confirms that ejections and sweeps dominate among all four events for both shear stresses in both geometries. $Q2^+$ and $Q4^+$ have the largest contribution in the generation of $\langle-\overline{u'w'}\rangle^+$, with $Q2^+$ being the largest. In the flow over $\lambda/k = 5.2$, consistent with the results of Toussaint *et al.* [10], $\widetilde{Q2}^+$ has the largest contribution to $\langle-\widetilde{u}\widetilde{w}\rangle^+$, while $\widetilde{Q4}^+$ has the largest contribution to $\langle-\widetilde{u}\widetilde{w}\rangle^+$ in the flow over $\lambda/k = 10.4$. This is due to significant water surface deformations in the $\lambda/k = 10.4$ case which generates larger spatial fluctuation of velocities than in the $\lambda/k = 5.2$ case and Toussaint *et al.* [10]. The contours of the normalized spanwise-averaged $Q2^+$ and $Q4^+$ events in Fig. 6 represent that the highest magnitude of the ejection and sweep events of the Reynolds shear stress occurs at around the roughness height with the maximum $Q2^+$ localized above the maximum $Q4^+$ event. Regions of strong ejection and sweep are established downstream of the trailing edge of each bar and expand in the wall-normal direction downstream of the bars. Due to the larger bar spacing in the flow over $\lambda/k = 10.4$, these regions extend to a larger x/k. This figure implies that the strong ejection and sweep events related to $\langle-\overline{u'w'}\rangle^+$ are induced only by the bars and that the water surface deformation does not have a significant contribution in the generation of these events. Figures 7(a) and 7(c) show, similarly, the negligible contribution of the deformed water surface to the generation of $\widetilde{Q2}^+$ and $\widetilde{Q4}^+$ in the flow over $\lambda/k = 5.2$. However, Figs. 7(b) and 7(d) reveal a more significant effect of the water surface deformation on inducing especially sweep events in the bulk flow over $\lambda/k = 10.4$. At the upstream of the standing wave, a relatively strong sweep event is established and extended downward to the bed, consistent with Figs. 5(b) and 5(d), where a strong positive $\langle\widetilde{u}\rangle^+$ and relatively strong negative $\langle\widetilde{w}\rangle^+$ are generated at the same location. This explains the reason that $\widetilde{Q4}^+$ has the largest contribution to $\langle-\widetilde{u}\widetilde{w}\rangle^+$ in the flow over $\lambda/k = 10.4$. To summarize, the negative $\langle\widetilde{w}\rangle^+$ induced by the downward motion of the water surface along with the large positive $\langle\widetilde{u}\rangle^+$ at the upstream of the standing wave lead to the generation

TABLE IV. Quadrant contribution to Reynolds and dispersive shear stress.

λ/k	Qi^+	Contribution to $\langle -\overline{u'w'}\rangle^+$	$\widetilde{\mathrm{Qi}}^+$	Contribution to $\langle -\widetilde{u}\widetilde{w}\rangle^+$
5.2	$\mathrm{Q1}^+(u'>0,\ w'>0)$	−21.2%	$\widetilde{\mathrm{Q1}}^+(\widetilde{u}>0,\widetilde{w}>0)$	−30.7%
5.2	$\mathrm{Q2}^+(u'<0,\ w'>0)$	84.8%	$\widetilde{\mathrm{Q2}}^+(\widetilde{u}<0,\widetilde{w}>0)$	83.1%
5.2	$\mathrm{Q3}^+(u'<0,\ w'<0)$	−28.5%	$\widetilde{\mathrm{Q3}}^+(\widetilde{u}<0,\widetilde{w}<0)$	−26.0%
5.2	$\mathrm{Q4}^+(u'>0,\ w'<0)$	64.9%	$\widetilde{\mathrm{Q4}}^+(\widetilde{u}>0,\widetilde{w}<0)$	73.6%
10.4	$\mathrm{Q1}^+(u'>0,\ w'>0)$	−30.1%	$\widetilde{\mathrm{Q1}}^+(\widetilde{u}>0,\widetilde{w}>0)$	−37.3%
10.4	$\mathrm{Q2}^+(u'<0,\ w'>0)$	96.6%	$\widetilde{\mathrm{Q2}}^+(\widetilde{u}<0,\widetilde{w}>0)$	68.6%
10.4	$\mathrm{Q3}^+(u'<0,\ w'<0)$	−40.7%	$\widetilde{\mathrm{Q3}}^+(\widetilde{u}<0,\widetilde{w}<0)$	−21.8%
10.4	$\mathrm{Q4}^+(u'>0,\ w'<0)$	74.2%	$\widetilde{\mathrm{Q4}}^+(\widetilde{u}>0,\widetilde{w}<0)$	90.5%

of strong downwash of the time-averaged flow through a $\widetilde{\mathrm{Q4}}^+$ event and locally large $\langle -\widetilde{u}\widetilde{w}\rangle^+$ in the flow over $\lambda/k = 10.4$. These lead to the generation of larger $\langle -\widetilde{u}\widetilde{w}\rangle^+$ above the bar crest in Fig. 3(b) and larger total contribution of the dispersive shear stress to f in the flow over $\lambda/k = 10.4$, which renders the combined effect of the water surface and bar spacing on the generation of the friction coefficient in the shallow flows.

To study the dynamics of the flow over the current roughness configuration, the double- (first temporal- and then spatial-) averaged streamwise momentum equation is calculated [2,3],

$$\frac{\partial\langle\overline{u}\rangle}{\partial t} + \langle\overline{w}\rangle\frac{\partial\langle\overline{u}\rangle}{\partial z} = \underbrace{-\frac{1}{\rho}\frac{\partial\langle\overline{p}\rangle}{\partial x} - \frac{1}{\rho}\left\langle\frac{\partial\widetilde{p}}{\partial x}\right\rangle}_{\text{Pressure Gradient(PG)}} + \underbrace{\nu\nabla^2\langle\overline{u}\rangle + \nu\langle\nabla^2\widetilde{u}\rangle}_{\text{Viscous Force(VF)}} + \underbrace{\frac{\partial\langle-\overline{u'w'}\rangle}{\partial z} + \frac{\partial\langle-\widetilde{u}\widetilde{w}\rangle}{\partial z}}_{\text{Turbulent Inertia(TI)}}. \quad (8)$$

The right-hand side of Eq. (8) is decomposed into three terms which contribute to the momentum transport. Turbulent inertia (TI) has been shown to constitute the dynamically most significant term in the mean momentum equation [41]. Where TI is positive, there is momentum source and the flow is accelerated, and where it is negative, there is momentum sink and the flow is decelerated. In similar decomposition of the RANS equation, TI is equal to the wall-normal gradient of the Reynolds shear stress, while applying DA methodology, the wall-normal gradient of the dispersive shear stress contributes to TI as well. Comparison of these two shear stress gradients gives a different perspective on the role of the dispersive shear stress in the mean dynamics of the flow [9]. Figure 8 shows the normalized wall-normal gradient of Reynolds and dispersive shear stresses and their sum, TI^+, over $\lambda/k = 5.2$ and $\lambda/k = 10.4$. The abrupt changes at $z/k = 1$ are due to the sudden change in the geometry function ϕ, which is multiplied with the shear stress gradients to account for the effects of the roughness. Unlike the previous works [8,9], the gradient of the dispersive shear stress is not equal to or larger than the gradient of the Reynolds shear stress, except around the bar height and near the water surface, and this is attributed to the difference in the roughness type and effects of the water surface. Under the crest of the bars, TI^+ and both its

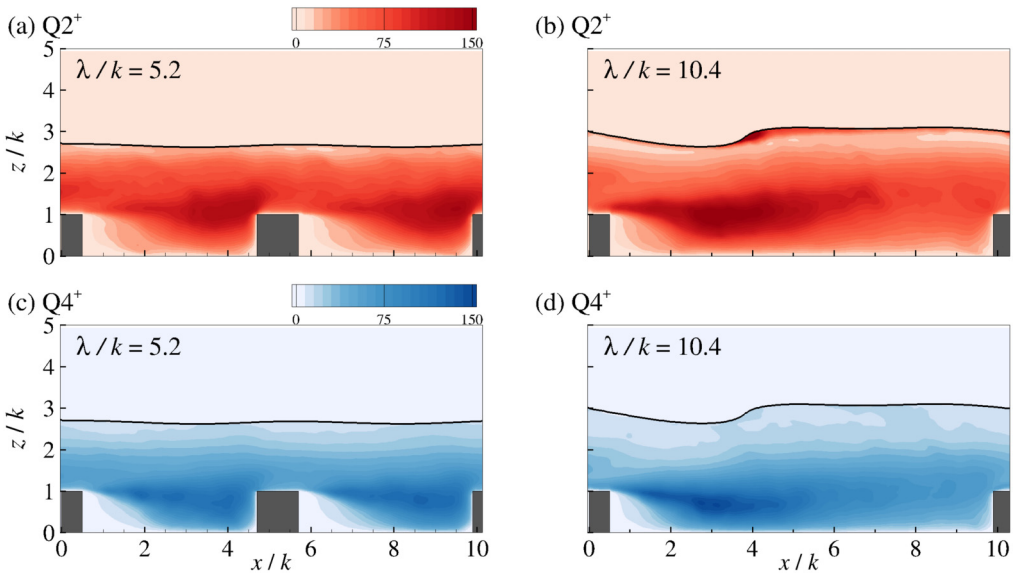

FIG. 6. Contours of spanwise-averaged (a),(b) $\mathrm{Q2}^+$ and (c),(d) $\mathrm{Q4}^+$ events.

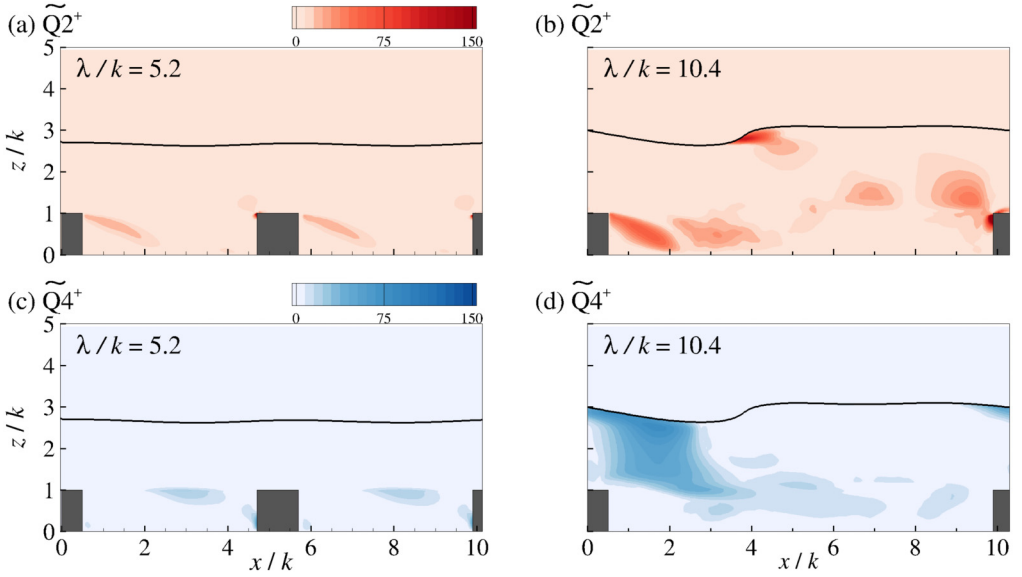

FIG. 7. Contours of spanwise-averaged (a),(b) $\widetilde{Q2}^+$ and (c),(d) $\widetilde{Q4}^+$ events.

components are positive, suggesting acceleration in the flow, while just above the bar, the flow is decelerated. A strong local form drag generated over the bars crest due to its square shape leads to this deceleration. The large negative magnitude of $\frac{\partial\langle-\widetilde{u}\widetilde{w}\rangle^+}{\partial z^+}$ at $z/k \approx 1$ contributes more than $\frac{\partial\langle-\overline{u'w'}\rangle^+}{\partial z^+}$ to the deceleration of the flow due to the sudden change in ϕ which leads to the large spatial fluctuations of flow quantities in this region. Above the roughness height, there is a local increase in $\frac{\partial\langle-\widetilde{u}\widetilde{w}\rangle^+}{\partial z^+}$, which is stronger in the flow over $\lambda/k = 10.4$, highlighting the interfering effect of the water surface in the distribution of $\langle-\widetilde{u}\widetilde{w}\rangle^+$ in the bulk of the fluid [Fig. 4(d)]. However, this local increase does not lead to the acceleration of the fluid as it is counteracted by a local negative peak of $\frac{\partial\langle-\overline{u'w'}\rangle^+}{\partial z^+}$. The flow is decelerated above the roughness crest. Near the water surface, the changes in TI^+ and its components is larger in the flow over $\lambda/k = 10.4$. The large changes in the water surface elevation lead to the generation of relatively large TI^+ and acceleration of the flow near the water surface in this case.

C. Kinetic energy

In order to investigate the effects of double averaging and the contribution of spatial variations in time-averaged velocities in the generation of kinetic energy, the DA total kinetic energy is calculated as

$$\frac{1}{2}\langle\overline{u_i}\overline{u_i}\rangle = \underbrace{\frac{1}{2}\langle\overline{u_i}\rangle\langle\overline{u_i}\rangle}_{\text{Mean Kinetic Energy(MKE)}} + \underbrace{\frac{1}{2}\langle\overline{u_i'u_i'}\rangle}_{\text{Turbulent Kinetic Energy(TKE)}} + \underbrace{\frac{1}{2}\langle\widetilde{u_i}\widetilde{u_i}\rangle}_{\text{Wake Kinetic Energy(WKE)}} . \quad (9)$$

Equation (9) is calculated by substituting u_i in the total kinetic energy $\frac{1}{2}(u_iu_i)$ using Eq. (3) and applying first temporal and then spatial averaging. The DA total kinetic energy is decomposed into three terms: the mean kinetic energy (MKE), turbulent kinetic energy (TKE), and wake kinetic energy (WKE), corresponding to the effects of the mean flow, the turbulent flow, and spatial variations of the time-averaged flow,

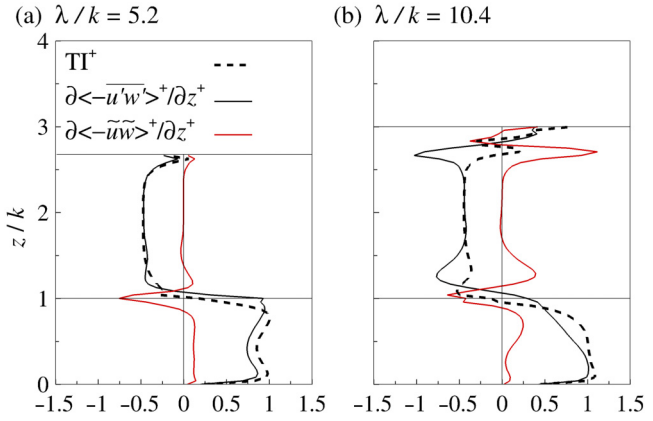

FIG. 8. Profiles of the wall-normal gradient of Reynolds and dispersive shear stresses.

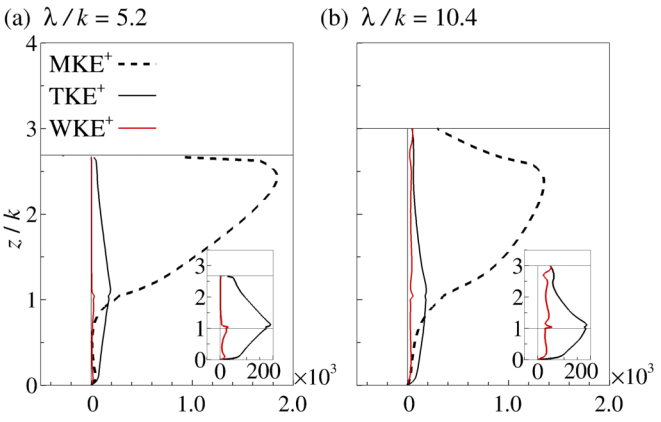

FIG. 9. Profiles of the mean, turbulent, and wake kinetic energy.

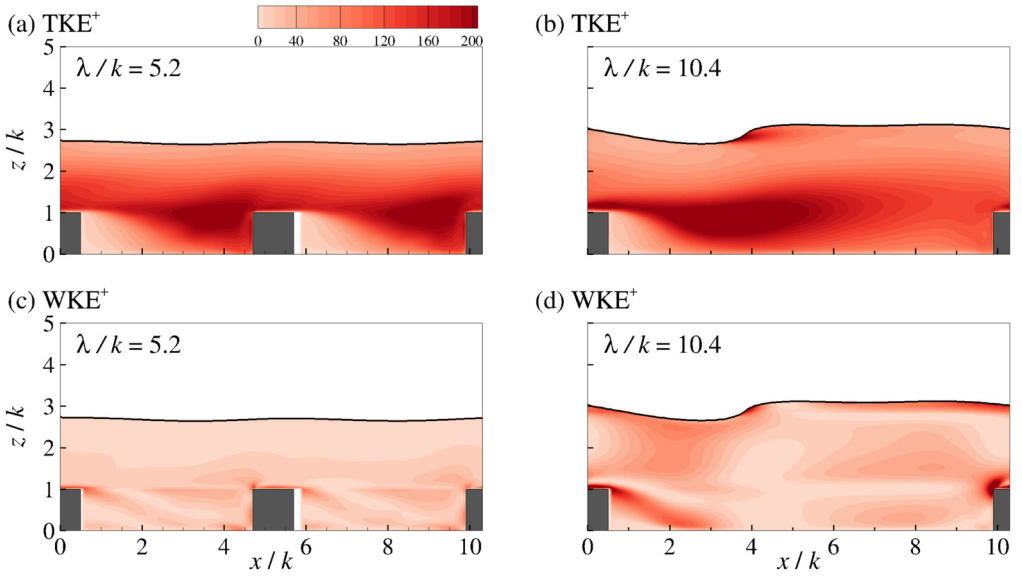

FIG. 10. Contours of spanwise-averaged (a),(b) turbulent and (c),(d) wake kinetic energy.

respectively. These contributions in percentage to the DA total kinetic energy for both geometries are provided in Table V. MKE has the largest and WKE has the smallest contribution. Increasing the bar spacing, the contribution of both TKE and WKE increases and that of MKE decreases. The normalized contributions are shown in the wall-normal direction in Fig. 9. The maximum MKE^+ occurs near the water surface, mainly due to the local increase in the mean streamwise velocity at the upstream of the standing wave near the water surface [30,39]. On the other hand, the maximum TKE^+ and WKE^+ occur at the bar crest as the sudden change in the geometry function ϕ leads to the enhancement of the temporal and spatial velocity fluctuations (Figs. 5(b) and 5(d), and [7,8,10]). Figure 10 presents contours of time- and spanwise-averaged normalized turbulent and wake kinetic energy. There is a high magnitude of turbulent kinetic energy at the height of the bar crest and a localized peak under the standing wave in the flow over $\lambda/k = 10.4$. The large magnitudes of WKE^+ are localized at the bar edges. In addition, for $\lambda/k = 10.4$, there is an area of relatively large WKE^+ at the upstream of the standing wave which corresponds to the local increase of $\langle\widetilde{u}\rangle^+$ and $\langle\widetilde{w}\rangle^+$ in Figs. 5(b) and 5(d). These figures suggest that similar to the Reynolds shear stress [Figs. 4(a) and 4(b)], the Reynolds normal stresses are enhanced by the presence of the bars and have local maxima at the bar height. The spatial variations of the normal stresses, however, are influenced by both the bar and the changes in the water surface elevation.

TABLE V. Mean, turbulent, and wake kinetic energy contribution to the total kinetic energy.

λ/k	MKE	TKE	WKE
5.2	88.1%	11.2%	0.7%
10.4	83.0%	12.9%	4.1%

IV. CONCLUSION

The results of large-eddy simulations of turbulent free-surface flow over spanwise-aligned square bars in an open channel flow have been analyzed to investigate the spatial variation of Reynolds and dispersive shear stresses and their effects on the streamwise momentum balance and the friction factor. Two bar spacings, corresponding to transitional and k-type roughness at similar Re and Fr, have been considered. The largest contribution to the friction factor f stems from the Reynolds shear stress in both geometries, while by increasing the bar spacing, this contribution decreases and that of the dispersive shear stress increases. This is due to the presence of the standing wave at the water surface in the flow over k-type roughness which generates a region of strong positive dispersive shear stress upstream of the wave extending from the water surface to the bed. The changes in the water surface elevation in this case, which is insignificant in the flow over transitional roughness, along with the roughness effects lead to the generation of stronger components of the dispersive shear stress, especially above the bar crest. Quadrant analysis has revealed that these strong components induce a downwash in the time-averaged flow at the upstream of the standing wave, leading to the larger contribution of dispersive shear stresses to the friction coefficient in this case. Furthermore, dominant ejection and sweep events of the Reynolds shear stress are not affected by the water surface and are only influenced by the roughness in both geometries. The sum of the wall-normal gradients of Reynolds and dispersive shear stresses has demonstrated that the mean flow accelerates under the bar crest and decelerates above it. The contribution of dispersive shear stress in the acceleration and deceleration of the flow is small, except near the bar crest and water surface. Near the bar crest, the dispersive shear stress contributes to the deceleration of the flow and, near the water surface, it contributes to the acceleration of the flow. The decomposition of the total kinetic energy has revealed the effects of mean, turbulent, and spatial variations of the time-averaged velocities.

The mean flow has the largest contribution and, by increasing the bar spacing, it decreases while the contribution of turbulent and wake kinetic energy increases. The large contribution of the turbulent kinetic energy is induced by the changes made by the roughness in the flow. Both the roughness and water surface contribute to the generation of wake kinetic energy. These results suggest that in flows with intermediate relative submergence and shallow flows, significant water surface deformation results in large spatial variation of the flow, and hence its time-averaged quantities. Modifying bed topography or relative submergence in engineering designs could be beneficial, for example, by reducing friction factors and hence energy consumption. In flow monitoring applications, examining the water surface deformation can be employed for predicting hydrodynamics of the flow, for example, the bulk flow and changes in relative submergence which are especially helpful in predicting extreme conditions such as flooding.

ACKNOWLEDGMENTS

Financial support was provided by the EPSRC/UK project "Rapid Monitoring of River Hydrodynamics and Morphology using Acoustic Holography," Grant No. EP/R022135/1. The simulations were carried out on UCL's high-performance computer Grace.

[1] J. Jiminez, Turbulent flows over rough walls, Annu. Rev. Fluid Mech. **36**, 173 (2004).
[2] N. R. Wilson and R. H. Shaw, A higher order closure model for canopy flow, J. Appl. Meteorol. **16**, 1197 (1977).
[3] M. Raupach and R. Shaw, Averaging procedures for flow within vegetation canopies, Boundary-Layer Meteorol. **22**, 79 (1982).
[4] V. I. Nikora, D. Goring, I. McEwan, and G. Griffiths, Spatially-averaged open-channel flow over a rough bed, J. Hydraul. Eng. **127**, 123 (2001).
[5] V. I. Nikora, I. McEwan, S. McLean, S. Coleman, D. Pokrajac, and R. Walters, Double-averaging concept for rough-bed open-channel and overland flows: Theoretical background, J. Hydraul. Eng. **133**, 873 (2007).
[6] P. Forooghi, A. Stroh, P. Schlatter, and B. Frohnapfel, Direct numerical simulation of flow over dissimilar, randomly distributed roughness elements: A systematic study on the effect of surface morphology on turbulence, Phys. Rev. Fluids **3**, 044605 (2018).
[7] J. Yuan and M. Aghaei Jouybari, Topographical effects of roughness on turbulence statistics in roughness sublayer, Phys. Rev. Fluids **3**, 114603 (2018).
[8] T. O. Jelly and A. Busse, Reynolds number dependence of Reynolds and dispersive stresses in turbulent channel flow past irregular near-Gaussian roughness, Intl. J. Heat Fluid Flow **80**, 108485 (2019).
[9] C. Manes, D. Pokrajac, O. Coceal, and I. McEwan, Significance of form-induced stress in rough wall turbulent boundary layers, Acta Geophys. **56**, 845 (2008).
[10] D. Toussaint, F. Chedevergne, and O. Léon, Analysis of the different sources of stress acting in fully rough turbulent flows over geometrical roughness elements, Phys. Fluids **32**, 075107 (2020).
[11] S. Okamoto, S. Seo, K. Nakaso, and I. Kawai, Turbulent shear flow and heat transfer over the repeated two-dimensional square ribs on ground plane, J. Fluids Eng. **115**, 631 (1993).
[12] L. Djenidi, R. Elavarasan, and R. A. Antonia, The turbulent boundary layer over transverse square cavities, J. Fluid Mech. **395**, 271 (1999).
[13] J. Cui, V. C. Patel, and C. L. Lin, Large-eddy simulation of turbulent flow in a channel with rib roughness, Intl. J. Heat Fluid Flow **24**, 372 (2003).
[14] T. Ikedaand P. Durbin, Direct numerical simulations of a rough-wall channel flow, J. Fluid Mech. **571**, 235 (2007).
[15] A. E. Perry, W. H. Schofield, and P. N. Joubert, Rough wall turbulent boundary layers, J. Fluid Mech. **37**, 383 (1969).
[16] R. L. Simpson, A generalized correlation of roughness density effects on the turbulent boundary layer, AIAA J. **11**, 242 (1973).
[17] J. Tani, *Turbulent Boundary Layer Development Over Rough Surfaces* (Springer, Berlin, 1987).
[18] M. Gad-el-Hak, *Flow Control: Passive, Active, and Reactive Flow Management* (Cambridge University Press, Cambridge, 2000).
[19] K. Fukagata, K. Iwamoto, and N. Kasagi, Contribution of Reynolds stress distribution to the skin friction in wall-bounded flows, Phys. Fluids **14**, L73 (2002).
[20] V. I. Nikora1, T. Stoesser, S. M. Cameron1, M. Stewart, K. Papadopoulos, P. Ouro, R. McSherry, A. Zampiron, I. Marusic, and R. A. Falconer, Friction factor decomposition for rough-wall flows: Theoretical background and application to open-channel flows, J. Fluid Mech. **872**, 626 (2019).
[21] N. Renard and S. Deck, A theoretical decomposition of mean skin friction generation into physical phenomena across the boundary layer, J. Fluid Mech. **790**, 339 (2016).
[22] R. Jalalabadi, J. Kim, and H. J. Sung, Turbulent structures in an optimal Taylor-Couette flow between concentric counter-rotating cylinders, J. Turbul. **18**, 480 (2017).
[23] R. Jalalabadi, J. Hwang, M. Nadeem, M. Yoon, and H. J. Sung, Turbulent boundary layer over a divergent convergent superhydrophobic surface, Phys. Fluids **29**, 085112 (2017).
[24] R. Jalalabadi and H. J. Sung, Influence of backflow on skin friction in turbulent pipe flow, Phys. Fluids **30**, 065104 (2018).
[25] T. Stoesser, Physically realistic roughness closure scheme to simulate turbulent channel flow over rough beds within the framework of LES, J. Hydraul. Eng. **136**, 812 (2010).
[26] S. Bomminayuni and T. Stoesser, Turbulence statistics in an open-channel flow over a rough bed, J. Hydraul. Eng. **137**, 1347 (2011).
[27] S. Kara, M. C. Kara, T. Stoesser, and T. W. Sturm, Free-surface versus rigid-lid LES computations for bridge-abutment flow, J. Hydraul. Eng. **141**, 04015019 (2015).
[28] T. Stoesser, R. McSherry, and B. Fraga, Secondary currents and turbulence over a non-uniformly roughened open-channel bed, Water **7**, 4896 (2015).
[29] R. McSherry, K. Chua, and T. Stoesser, Large eddy simulation of free-surface flows, J. Hydrodyn. **29**, 1 (2017).

[30] R. McSherry, K. Chua, T. Stoesser, and S. Mulahasan, Free surface flow over square bars at intermediate relative submergence, J. Hydraul. Res. **56**, 825 (2018).

[31] F. Nicoud and F. Ducros, Subgrid-scale stress modelling based on the square of the velocity gradient tensor, Flow Turbul. Combust. **62**, 183 (1999).

[32] M. Sussman, P. Smereka, and S. Osher, A level set approach for computing solutions to incompressible two-phase flow, J. Comput. Phys. **114**, 146 (1994).

[33] J. A. Sethian and P. Smereka, Level set methods for fluid interfaces, Annu. Rev. Fluid Mech. **35**, 341 (2003).

[34] M. Cevheri, R. McSherry, and T. Stoesser, A local mesh refinement approach for large-eddy simulations of turbulent flows, Intl. J. Numer. Meth. Fluids **82**, 261 (2016).

[35] P. Ouro, B. Fraga, U. Lopez-Novoa, and T. Stoesser, Scalability of an Eulerian-Lagrangian large-eddy simulation solver with hybrid MPI/OpenMP parallelisation, Comput. Fluids **179**, 123 (2019).

[36] S. E. Coleman, V. I. Nikora, S. R. McLean, and E. Schlicke, Spatially averaged turbulent flow over square ribs, J. Eng. Mech. **133**, 194 (2007).

[37] D. Pokrajac, L. J. Campbell., V. Nikora, C. Manes, and I. McEwan, Quadrant analysis of persistent spatial velocity perturbations over square-bar roughness, Expt. Fluids **42**, 413 (2007).

[38] T. O. Jelly and A. Busse, Reynolds and dispersive shear stress contributions above highly skewed roughness, J. Fluid Mech. **852**, 710 (2018).

[39] R. Jalalabadi, T. Stoesser, P. Ouro, Q. Luo, and Z. Xie, Free surface flow over square bars at different Reynolds numbers, J. Hydro-envir. Res. **36**, 67 (2021).

[40] J. M. Wallace, Quadrant analysis in turbulence research: History and evolution, Annu. Rev. Fluid Mech. **48**, 131 (2016).

[41] C. Chin, J. Philip, J. Klewicki, A. Ooi, and I. Marusic, Reynolds-number-dependent turbulent inertia and onset of log region in pipe flows, J. Fluid Mech. **757**, 747 (2014).